



Engineering CeO₂ configurations to regulate the CuO_x dispersion and switch pathways of preferential CO oxidation

Junfang Ding^{a,1}, Changjin Xu^{b,1}, Guilan Fan^a, Tuya Naren^a, Yan Wang^{a,c}, Yang Liu^a,
Xiaojun Gu^{a,*}, Limin Wu^{a,d,**}, Shanghong Zeng^{a,*}

^a School of Chemistry and Chemical Engineering, Inner Mongolia University, Hohhot 010021, China

^b College of Pharmacy, Inner Mongolia Medical University, Hohhot 010110, China

^c State Key Laboratory of Baiyunobo Rare Earth Resource Researches and Comprehensive Utilization, Baotou Research Institute of Rare Earths, Baotou 014030, China

^d Department of Materials Science and State Key Laboratory of Molecular Engineering of Polymers, Fudan University, Shanghai 200433, China

ARTICLE INFO

Keywords:

Crystal plane effect
Atomic arrangement
Highly-dispersed CuO_x
Reaction pathway
Preferential oxidation of CO

ABSTRACT

Constructing highly dispersed catalysts is of tremendous interest for catalysis. However, the mechanism and avenue to tune dispersive behavior and thus reactivity of supported catalysts is still facing challenges. Herein, we manipulate crystal plane-induced CeO₂ configurations toward improved CuO_x dispersion, and investigate the structural evolution and reaction intermediates during the CO preferential oxidation over CuO_x/CeO₂ catalysts. Results demonstrate that the optimal atomic arrangement appears on nanosphere-shaped CeO₂ with exposed {111} and {100} facets in contrast to nanorod-shaped CeO₂ exposed {100} and {110} facets and nanowire-shaped CeO₂ exposed {110} facets. By combining theoretical simulations and systematic characterizations including *in situ* DRIFTS, *in situ* Raman spectra and XAFS, it reveals the optimal catalyst favors the formation of highly dispersed CuO_x with surface-enriched Cu⁺, which is highly active site for catalysis. Furthermore, *in situ* Raman spectra provide direct evidence that the optimal support configuration facilitates the lattice oxygen extraction, thus promoting the carboxyl pathway.

1. Introduction

Investigations of heterogeneous catalysts have mainly focused on improving their activity, selectivity, and stability in the past decades. Heterogeneous catalysis involves a series of fundamental reaction steps, including adsorption of reactants, the diffusion of intermediate species, transformation of chemical bonds, and desorption of final products [1, 2]. Each step is closely related to the surface chemistry of oxide and metal nanoparticles on the catalyst [3,4]. Thus, modifying the dispersion and reactivity of supported oxide/metal nanoparticles is desirable but remains challenging. Inspired by the enzyme catalysis in nature, where the catalytically active center is highly distributed on the atomic level. Designing highly dispersed oxide/metal nanoparticles on the supports with rational atomic arrangement allows to stabilize active sites in unique support configuration, where the atomic arrangement of support is responsible for the enhancement of dispersibility, lattice oxygen transfer and catalytic performance.

Ceria-containing catalysts, owning excellent oxygen storage, superior redox properties and accessible oxidation states, are among the most attractive heterogeneous catalysts in many reactions involving surface science, such as CO/CO₂ hydrogenation [5,6], water gas shift reaction [7], CO oxidation [8], and preferential oxidation of CO (CO-PROX) [9]. The catalytic performance of CuO/CeO₂ composites is mainly associated with the fine-dispersed copper species, synergistic interactions between two oxides arising from complex redox effects at the interfacial perimeter [9–11]. The redox effects include electron exchange between the Ce⁴⁺/Ce³⁺ and Cu²⁺/Cu⁺ redox pairs, and formation of surface oxygen vacancies [9,10]. It has been proposed that active sites in CuO-CeO₂ system for CO oxidation are related to fine-dispersed Cu⁺ species [9,11, 12]. Since Cu⁺ species mainly generated by the interfacial redox interactions between CuO_x and CeO₂, highly dispersed CuO_x particles provides the highest reducibility to CuO_x/CeO₂ mixtures, thus facilitating the formation of Cu⁺ species at interfacial perimeter. Therefore, surface chemistry and dispersion of supported CuO_x has a profound

* Corresponding authors.

** Corresponding author at: School of Chemistry and Chemical Engineering, Inner Mongolia University, Hohhot 010021, China.

E-mail addresses: xiaojun.gu@imu.edu.cn (X. Gu), lmw@fudan.edu.cn (L. Wu), zengshanghong@imu.edu.cn (S. Zeng).

¹ Junfang Ding and Changjin Xu contributed equally and should be considered co-first authors.

influence on catalytic activity and selectivity, which is determined by the configuration of CeO_2 support.

To optimize the configuration of CeO_2 support, CeO_2 nanocrystals exposed different crystal facets were controllably synthesized, and the effect of crystal facets on catalytic performance have been studied in different reactions [13,14]. For instance, the CuO supported on CeO_2 thin films exposing $\{100\}$ facet exhibits higher activity for CO oxidation than that on CeO_2 $\{111\}$ crystal facet, attributable that CeO_2 $\{100\}$ facet assists the change of copper valence [15]. The Cu/CeO_2 nanorods with $\{100\}$ and $\{110\}$ planes have better catalytic performance than the nanocube and nanopolyhedra samples [16]. However, hydrogenation reaction shows an opposite trend, and CeO_2 $\{111\}$ as low-vacancy surface promotes CO hydrogenation [15]. Another example appeared in the dephosphorylation reaction, and the reactivity follows the order $\{111\} > \{110\} > \{100\}$ for CeO_2 configuration [17]. Similarly, we have shown that the polycrystalline CuO/CeO_2 spheres and spindles exposed $\{111\}$ and $\{002\}$ crystal facets have excellent catalytic performance for CO-PROX due to the highest proportion of oxygen vacancies at the intersection of CeO_2 $\{111\}$ and $\{002\}$ facets [18]. Based on the above, an in-depth understanding of the nature of CeO_2 configuration has a great advantage in the design of the specific structure of nanomaterials for heterogeneous catalysis. However, the influence of the dispersion of CuO_x , extraction of lattice oxygen, $\text{CuO}_x\text{-CeO}_2$ interaction and reaction intermediates on catalytic performance due to the configurational discrepancy has not been well elucidated in prior studies, remained a major challenge.

To resolve this unsettled dilemma, herein, a designability strategy is reported to load CuO_x on three different CeO_2 configurations by employing the impregnation and hydrothermal methods, respectively, and we hope to establish the trade-off relationship between support configuration, CuO_x dispersion, reaction intermediates and catalytic performance. The high CuO_x dispersion and greatly enhanced interactions are discovered on the nanosphere-shaped CeO_2 support with the exposed $\{111\}$ and $\{100\}$ facets, as evidenced by XRD, H_2 -TPR, XAFS and theoretical calculations, and these enabling high CO-PROX performance. Assisted by the combination of spectroscopic techniques, molecular-scale insights into the underlying catalytic mechanism are achieved by monitoring the active surface species and structural evolution under CO-PROX reaction condition. Complementary *in situ* DRIFT and *in situ* Raman spectra reveal the molecular mechanism of lattice oxygen extraction through a carboxyl pathway on this optimal support configuration.

2. Experimental section

2.1. Synthesis of CeO_2 with different morphologies

$\text{Ce}(\text{NO}_3)_3 \cdot 6\text{H}_2\text{O}$ (2.0 g) was dispersed in the mixed solution of 2 mL of deionized water, 2 mL of glacial acetic acid and 52 mL of glycol and then the mixture reacted at 180°C for 200 min in a Teflon-lined steel autoclave. The resultant solid was calcined at 350°C for 4 h in air, leading to the CeO_2 nanospheres (noted as $\text{CeO}_2\text{-NS}$).

35 mL of NaOH (15.4 g) solution was added dropwise to 5 mL of $\text{Ce}(\text{NO}_3)_3 \cdot 6\text{H}_2\text{O}$ (1.5 g) solution and then the mixture reacted at 120°C for 72 h in a Teflon-lined steel autoclave. The resultant solid was calcined at 350°C for 4 h in air, leading to the CeO_2 nanowires (noted as $\text{CeO}_2\text{-NW}$).

35 mL of NaOH (8.4 g) solution was added dropwise to 5 mL of $\text{Ce}(\text{NO}_3)_3 \cdot 6\text{H}_2\text{O}$ (0.868 g) solution and then the mixture reacted at 100°C for 24 h in a Teflon-lined steel autoclave. The resultant solid was calcined at 350°C for 4 h in air, leading to the CeO_2 nanorods (noted as $\text{CeO}_2\text{-NR}$).

2.2. Synthesis of $\text{CuO}_x/\text{CeO}_2$ catalysts

In a typical impregnation process, CeO_2 (0.5 g) supports with three morphologies aforementioned were added to 30 mL of $\text{Cu}(\text{NO}_3)_2 \cdot 3\text{H}_2\text{O}$

(2.7 mg/mL) solution under stirring. This solution was stirred and aged for 12 h, and the resulting mixture was dried at 80°C overnight. Subsequently, the products were calcined at 500°C for 2 h, and as-synthesized samples were denoted as $\text{CuO}_x/\text{CeO}_2(\text{I})$.

In order to explore the generality of the crystal plane effect, the combination of the hydrothermal reaction of CeO_2 with three morphologies and $\text{Cu}(\text{NO}_3)_2 \cdot 3\text{H}_2\text{O}$ and the subsequent high-temperature calcination gave three catalysts. In detail, CeO_2 supports (0.5 g) with three morphologies and 16 mL of alcohol solution of $\text{Cu}(\text{NO}_3)_2 \cdot 3\text{H}_2\text{O}$ (0.080 g) reacted at 120°C for 12 h in a Teflon-lined steel autoclave. The resultant solids were calcined at 500°C for 2 h, resulting in $\text{CuO}_x/\text{CeO}_2(\text{H})$.

2.3. Ex situ characterization

Powder X-ray diffraction (XRD) patterns were obtained on a PANalytical X'pert PRO diffractometer using $\text{Cu K}\alpha$ radiation. Scanning electron microscopy (SEM) was performed on a Hitachi S-4800 scanning electron microscope. Transmission electron microscopy (TEM) and energy-dispersive X-ray spectroscopy (EDS) were conducted on a Tecnai G2S-TwinF20 apparatus. Aberration corrected scanning transmission electron microscopy (AC-STEM) was recorded on Titan Themis 60–300. The N_2 adsorption and desorption isotherm curves of the catalysts were measured on a Micromeritics ASAP2020 adsorption facility. The X-ray photoelectron spectroscopy (XPS) and Auger electron spectroscopy (AES) were obtained on a Thermo ESCALAB 250XI spectrometer. The Raman spectra were collected on a LABRAM-HR Confocal Laser Raman spectrometer with an excitation wavelength of 514 nm. Fourier transform-infrared spectra (FT-IR) were collected using a Nicolet iS50 FT-IR spectrometer. The X-ray absorption fine structure spectra (Cu K-edge) were collected at 1W1B station in Beijing Synchrotron Radiation Facility (BSRF). Using Si (111) double crystal monochromator, the data collection was carried out in transmission mode using ionization chamber. To obtain the quantitative structural parameters around central atoms, least-squares curve parameter fitting was performed using the Artemis (version 0.9.26). $\chi(k)$ exported from Athena was imported into the Hama Fortran code for Wavelet Transform analysis. The parameters were listed as follow: R range, $1\text{--}4\text{ \AA}$, k range, $0\text{--}13\text{ \AA}^{-1}$; k weight, 2; and Morlet function with $\kappa = 10$, $\sigma = 1$ was used as the mother wavelet to provide the overall distribution. Hydrogen temperature-programmed reduction experiments (H_2 -TPR) were carried out using a Micromeritics AutoChem II 2920 Apparatus equipped with thermal conductivity detector (TCD).

2.4. In situ characterization

Diffuse reflectance infrared Fourier transform spectroscopy (DRIFTS) was collected on a Nicolet iS50 spectrometer equipped with an MCT detector. Initially, 10 mg of the sample was purged in pure N_2 at a flow rate of $40\text{ mL}\cdot\text{min}^{-1}$ for 30 min at room temperature to remove water and adsorbed carbon species, and then the background spectra were collected for spectral correction. Subsequently, the reaction gasses (1% CO , 1% O_2 , 50% H_2 and He as balance gas), were introduced into the *in-situ* chamber at a flow rate of $10\text{ mL}\cdot\text{min}^{-1}$. *In situ* Raman spectra were obtained on a Horiba LabRAM HR Evolution micro-Raman spectrometer with an excitation wavelength of 633 nm. 50 mg of the catalyst was loaded into the sample holder specially designed to investigate structural evolution during the reaction. Then, a mixture consisting of 1.0 vol% CO , 1.0 vol% O_2 and 98 vol% N_2 was introduced into a gas control system, and the Raman spectra were recorded at specific temperatures.

2.5. Density functional theory calculations

Periodic density functional theory (DFT) calculations with spin unrestriction were performed using DMol3 module in Materials Studio

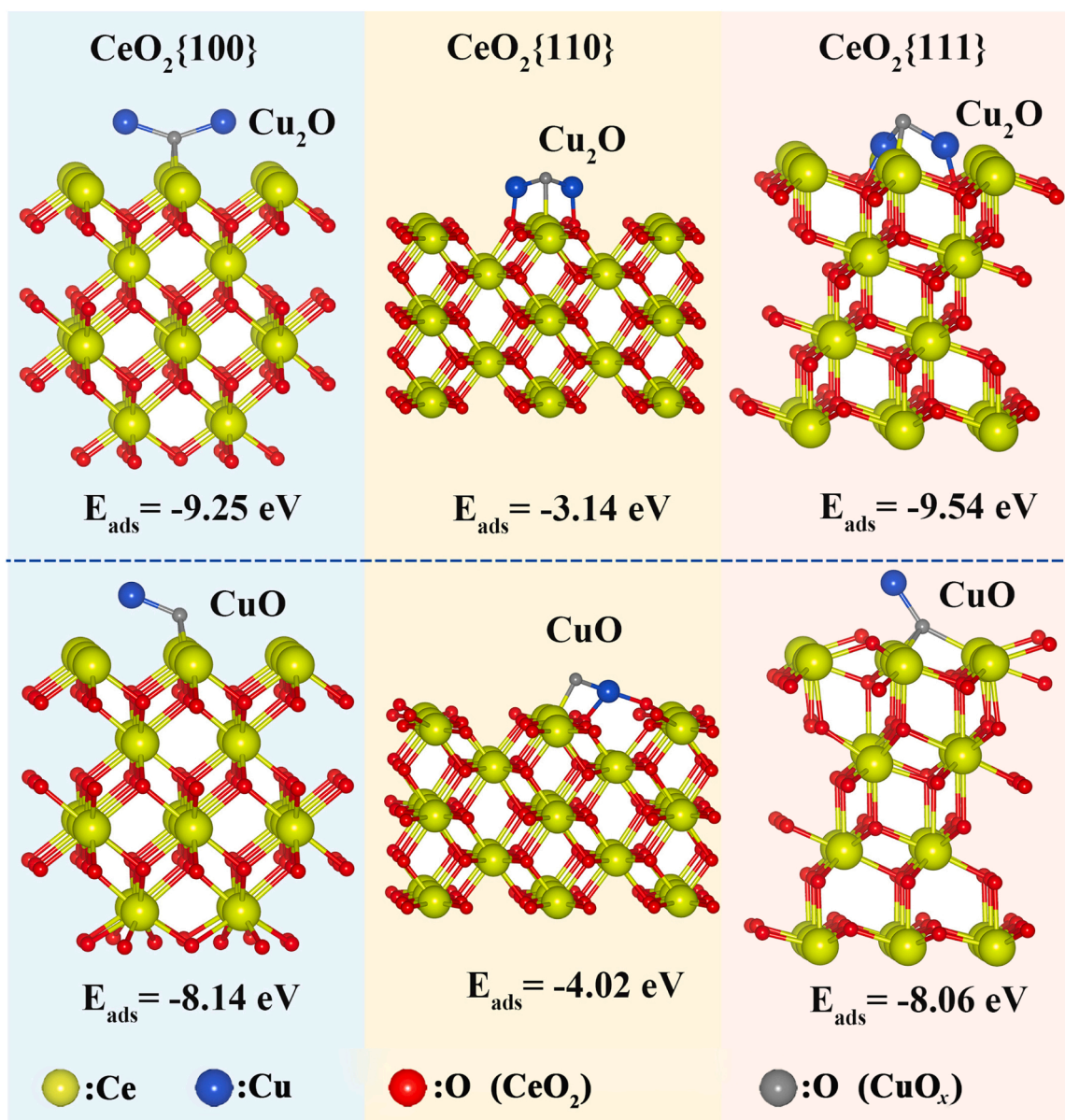


Fig. 1. Optimized adsorption configurations of Cu_2O and CuO on $\text{CeO}_2\{100\}$, $\{110\}$ and $\{111\}$ surfaces.

software package. The Perdew-Burke-Ernzerhof (PBE) functional of generalized gradient approximation (GGA) was employed for exchange correlation potential. The local double-numerical basis sets with polarization functions (DNP) were applied for valence orbitals, and DFT semi-core pseudopotential was used to treat the core electrons of metallic species. To obtain the accurate electronic density, a $(3 \times 3 \times 1)$ k-point mesh was chosen to perform the surface Brillouin zone. The geometry optimization was carried out under the convergence tolerance of the energy change (2×10^{-5} Ha), the maximum force (0.004 Ha/Å) and the maximum displacement (0.005 Å). The $\text{CeO}_2\{111\}$, $\text{CeO}_2\{110\}$ and $\text{CeO}_2\{100\}$ slabs were built with five O-Ce-O layers in 2×2 supercell, five Ce-O layers in 2×2 supercell and four Ce-O two-atoms layers in 2×2 supercell, respectively. A 15 Å vacuum space along the z-direction was added to avoid the interaction between the repeated slabs. The adsorption energies of CuO and Cu_2O molecules were described by $E_{\text{ads}} = E_{\text{adsorbate/slab}} - E_{\text{slab}} - E_{\text{adsorbate}}$, where $E_{\text{adsorbate/slab}}$, E_{slab} and $E_{\text{adsorbate}}$ are the total energy for the adsorbate-slab complex, the isolated slab and the isolated CuO or Cu_2O molecule, respectively.

2.6. Catalytic performance studies in CO-PROX

The CO-PROX catalytic performances were measured in a fixed-bed quartz reactor with a space velocity of $40,000 \text{ mL} \cdot \text{g}_{\text{cat}}^{-1} \cdot \text{h}^{-1}$ at atmospheric pressure. The feeding gas was composed of 1.0 vol% CO, 1.0 vol% O_2 , 50.0 vol% H_2 and N_2 balance. Here, 100 mg of catalyst power (180–200 meshes) was mixed with 200 mg quartz sand to eliminate the external mass transfer. The catalytic experiments were operated from room temperature to 215°C . The reactants and products were analyzed using a GC-2014 C gas chromatograph equipped with thermal conductivity detector. After the used catalyst underwent re-oxidation at 500°C for 2 h in air, the reusability was evaluated. Additionally, its stability was tested in reaction mixture (1% CO, 1% O_2 and 50% H_2 with N_2 as balance gas) at 135°C .

3. Results and discussion

3.1. DFT prediction of crystal plane effect on CuO_x stabilization

The exposure of specific facets can shape catalytic performance

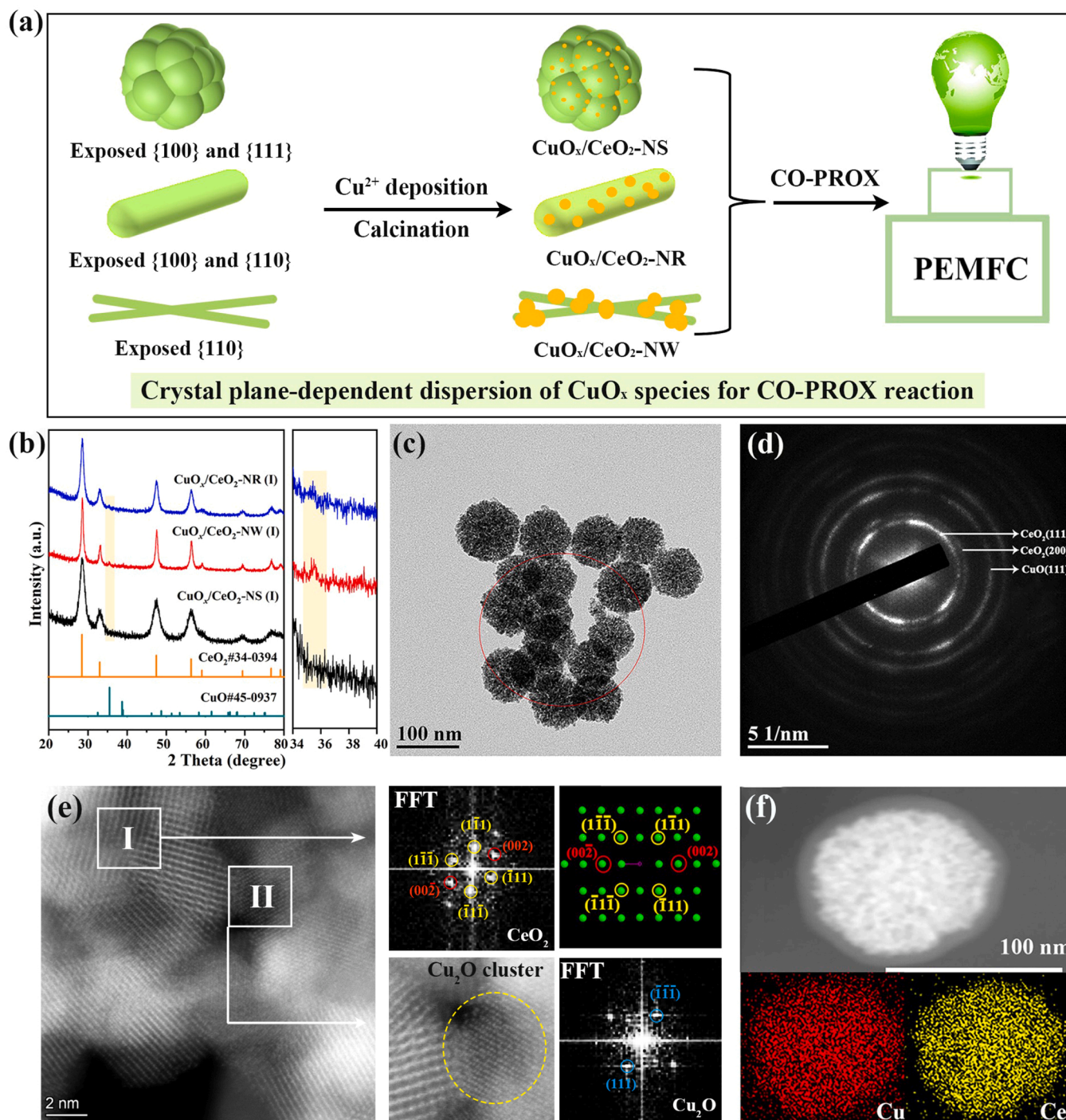


Fig. 2. Structural and morphological characterizations of the $\text{CuO}_x/\text{CeO}_2$ (I) catalysts: (a) Schematic illustrations of crystal plane-dependent dispersion of CuO_x species for CO-PROX reaction; (b) XRD patterns of all $\text{CuO}_x/\text{CeO}_2$ (I) samples; (c) TEM image; (d) electron diffraction patterns; (e) AC-STEM image, enlarged images of the special areas II, and FFT patterns in the rectangle regions; (f) STEM image and corresponding elemental mapping analysis of the $\text{CuO}_x/\text{CeO}_2$ -NS(I) catalyst.

through regulating surface oxygen reactivity and active species-support interaction. Here, $\text{CuO}_x/\text{CeO}_2$ as paradigm allows us to explore how to control the surface chemistry of CuO_x in CO-PROX. Initially, we performed DFT calculations to provide an understanding of CuO_x adsorption strength on CeO_2 crystal facets. Fig. 1 presents optimized adsorption configurations of Cu_2O and CuO on CeO_2 {100}, {110} and {111} surfaces, respectively. Theoretical simulations reveal that the adsorption energies (E_{ads}) of Cu_2O and CuO on CeO_2 {110} plane are -3.14 eV and -4.02 eV, respectively. Contrastively, the E_{ads} values of CuO_x on CeO_2 {100} and {111} reduce to more negative values. Wherein, the E_{ads}

values of Cu_2O on CeO_2 {100} and CeO_2 {111} are -9.25 eV and -9.54 eV, respectively, and the E_{ads} values of CuO on CeO_2 {100} and CeO_2 {111} are -8.14 eV and -8.06 eV, respectively. Given this, it can be predicted that CeO_2 {100} and {111} planes are more favorable for stabilizing CuO_x species, and thus constructing highly dispersed $\text{CuO}_x/\text{CeO}_2$ catalysts. Note that the E_{ads} values of Cu_2O on CeO_2 {100} and {111} surfaces are more negative relative to those of CuO . The stronger Cu_2O adsorption may result in the high coverage of Cu_2O on CeO_2 {100} and {111} surfaces. Interestingly, Cu^+ was generally proposed to be key active species for the CO-PROX reaction [9,12]. Consequently, the

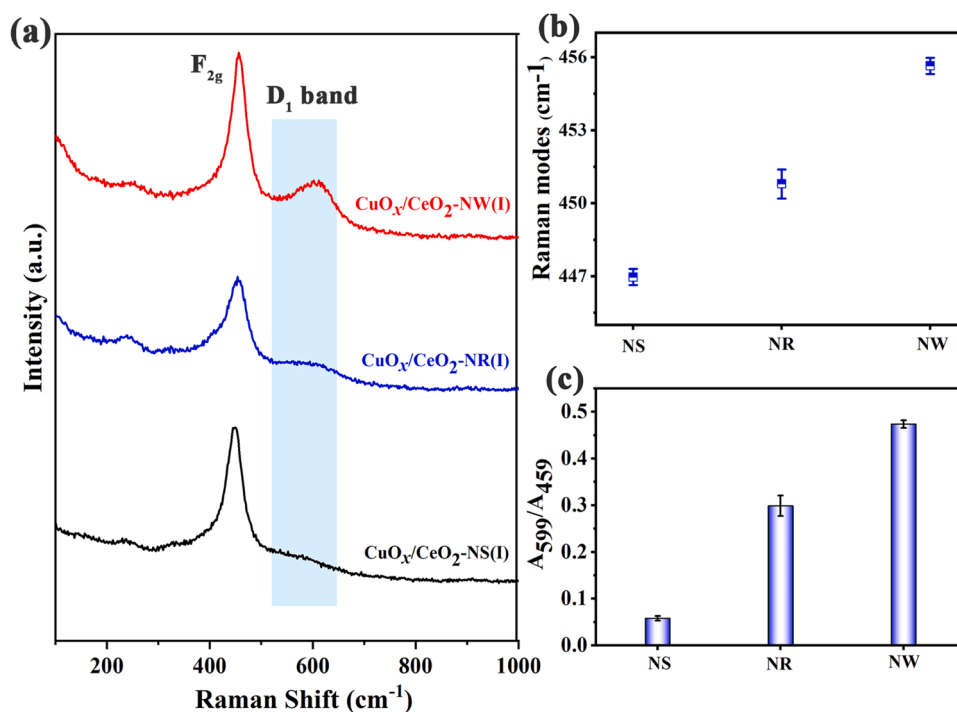


Fig. 3. Defect-related microstructure of the CuO_x/CeO₂(I) catalysts: (a) *Ex situ* Raman spectra; (b) location of F_{2g} modes; (c) corresponding ratio of A_D/A_{F2g} in the CuO_x/CeO₂(I) samples.

discrepancy in E_{ads} could result significant difference in catalytic performance.

Inspired by that, to construct the CeO₂ with different exposed crystal facets, the CeO₂ supports were prepared and characterized by XRD, TEM and HRTEM. The diffraction peaks in the CeO₂ supports at 2θ of 28.6, 33.2, 47.5 and 56.7° (Fig. S1) are ascribed to (111), (200), (220), and (311) planes of the cubic-fluorite CeO₂ (space group $Fm-3m$, JCPDS, No. 34-0394), respectively. In addition, TEM images (Fig. S2) have shown that CeO₂ supports with three morphologies were successfully synthesized. In more detail, HRTEM image of the CeO₂-NW clearly observes a hexagonal symmetry diffraction spot, corresponding to the {110} plane. Comparatively, Fourier transform pattern of CeO₂-NR exhibits three sets of diffraction spots, signifying that the CeO₂-NR exposes {100} and {110} facets. Two surface terminating planes assigned to (200) and (111) are observed with respective interplanar spacing of 0.28 and 0.31 nm in HRTEM image of the CeO₂-NS, suggesting that the exposed facets of CeO₂-NS are {100} and {111} facets. Based on aforementioned DFT calculation results, it can be speculated that the CeO₂-NS support facilitates stabilization of CuO_x active species on the surfaces.

3.2. Geometric structures and defect-related property of CuO_x/CeO₂

CuO_x/CeO₂ catalysts with three morphologies were synthesized to investigate crystal facet effect of the CeO₂ on the supported CuO_x species, as illustrated in Fig. 2a. The characteristic diffraction peaks of the CuO_x/CeO₂(I) catalysts (Fig. 2b) agree well with the CeO₂ crystalline phase with a cubic fluorite-type structure. In addition to CeO₂, a less pronounced diffraction peak corresponding to CuO is also observed at 35.6° in the CuO_x/CeO₂-NW(I) and CuO_x/CeO₂-NR(I) catalysts. Conversely, this diffraction peak is absent in the CuO_x/CeO₂-NS(I) sample because the size of CuO is below the detection limit. This observation suggests that the CuO_x species are more highly dispersed on the nanosphere-shaped CeO₂ supports than those on the nanorod and nanowire counterparts. Based on this result and combined with the following HRTEM analysis, it confirms the rationality of the DFT models and assumptions drawn from DFT prediction [19].

SEM images in Fig. S3 manifest that the CuO_x/CeO₂ catalysts preserve morphological characteristics of supports, but their surfaces become rough owing to the distribution of CuO_x species on the surfaces. In the case of CuO_x/CeO₂-NS(I), the nanosphere consists of the nanoparticles with a crystallite size of approximately 5 nm (Fig. 2c). FFT patterns in the region I (Fig. 2e) exhibit three sets of symmetry diffraction spots, which can be indexed to the (111) and (200) crystal planes of CeO₂, as evidenced by the selected area electron diffraction (SAED) in Fig. 2d. In the region II, the diffraction spots are assigned to the (111) crystal facets of Cu₂O with the corresponding interplanar spacing of 0.24 nm. The lattice fringes of Cu₂O and CeO₂ coherently extend along the interface and form an integration despite the presence of lattice mismatch, suggesting that the Cu₂O cluster (about 3 nm) has been embedded in the CeO₂ support. The signals of Cu and Ce are uniformly distributed in the EDS mapping images (Fig. 2f), demonstrating a high dispersion of CuO_x species in the CuO_x/CeO₂-NS(I) catalyst, in good agreement with the DFT and XRD results. Notably, the CuO_x/CeO₂-NS(I) with the exposed {111} and {100} facets possesses the largest BET surface area among the as-prepared samples (Table S1 and Fig. S4), facilitating the dispersion of CuO_x species. To prove the assumption of engineering CeO₂ configurations to regulate the CuO_x dispersion, the CeO₂ spindles with the exposed {111} and {100} facets were synthesized for loading CuO_x (Fig. S5a-c). The specific surface area of CuO_x/CeO₂ spindles (Fig. S5e-f) is 27.5 m²/g, close to the value of 22.3 m²/g for CuO_x/CeO₂ nanowires with the exposed {110} facets and low dispersion of CuO_x. The characteristic peaks of the CuO_x species were not detected in the XRD pattern of CuO_x/CeO₂ spindles (Fig. S5d), indicating that the CuO_x species are highly dispersed on the CeO₂ spindles. This phenomenon suggests that the dispersion of CuO_x species is mainly related to the exposed crystal facets of CeO₂ supports in the as-studied system. Of course, the specific surface area of CeO₂ supports also contributes to the dispersion of CuO_x.

The vibrational modes of Raman spectra, sensitive to the presence of defects in the metal oxides, are used to probe the vibration of metal-oxygen bond and the defect of catalysts [20]. A strong band in all CuO_x/CeO₂(I) catalysts appear at about 450 nm⁻¹ (Fig. 3a),

Table 1Chemical state and catalytic performance of the CuO_x/CeO₂(I) catalysts.

Sample	Cu/Ce ^a (Atomic ratio)	^b I _{sat} /I _{mp}	^c Cu ⁺	^d Ce ³⁺	^e I _{OH} /I _{M-O}	T _{50%} (°C)	^f Temperature window (°C)
CuO _x /CeO ₂ -NR(I)	0.23	0.41	0.17	0.21	0.96	81	135–215
CuO _x /CeO ₂ -NW(I)	0.30	0.48	0.09	0.22	0.83	162	–
CuO _x /CeO ₂ -NS(I)	0.19	0.36	0.24	0.19	1.04	65	95–215

^a Determined by XPS; ^b Estimated from area intensity analysis of the satellite peaks to main peaks; ^c Calculated using the equation of Cu⁺ % = (A – (A1/B) B)/(A+B) × 100; ^d Calculated by Ce³⁺/(Ce³⁺ + Ce⁴⁺); ^e Calculate by FT-IR spectra; ^f CO conversion more than 99%.

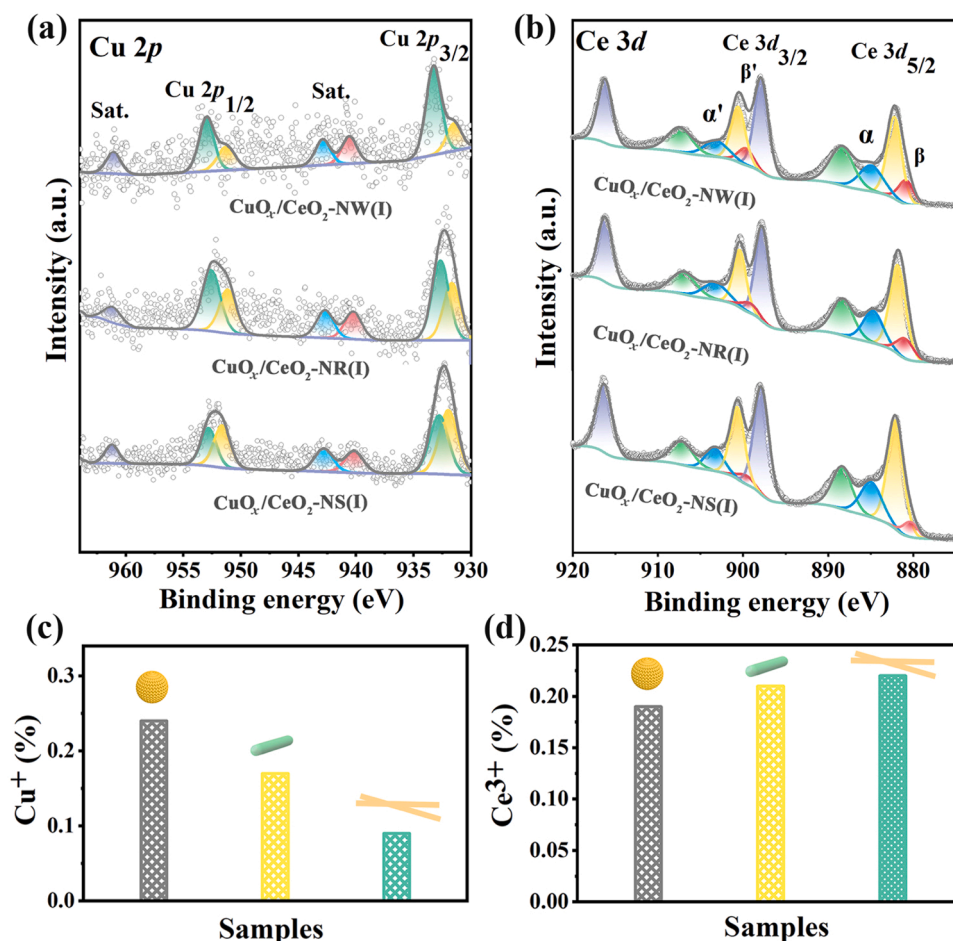


Fig. 4. High-resolution XPS spectra of (a) Cu 2p and (b) Ce 3d of the CuO_x/CeO₂(I) catalysts; Proportion of (c) Cu⁺ and (d) Ce³⁺ from XPS on the CuO_x/CeO₂(I) surfaces.

characteristic of the F_{2g} symmetric stretch mode in the cubic-fluorite CeO₂ structure, reflecting its structural dominance, in agreement with the XRD results [21]. Note that a clear shift of F_{2g} Raman band (Fig. 3b) is observed in the catalysts compared to the pristine CeO₂ (464 cm⁻¹) [22]. This phenomenon reveals the modification of Ce-O force constants and the change of the bond strengths due to the interaction of copper species and CeO₂ at the interface. Meanwhile, the defect-induced D modes of CeO₂ appear at 600 cm⁻¹, where the oxygen vacancies arise from the transfer of oxygen ions from their lattice sites to interstitial sites [23]. As shown in Fig. 3c, the concentration of oxygen vacancies was estimated by the A_D/A_{F2g}, following the sequence of CuO_x/CeO₂-NS(I) < CuO_x/CeO₂-NR(I) < CuO_x/CeO₂-NW(I). This is closely related to oxygen vacancy formation energy which follows the proposed order of {110} < {100} < {111} surfaces [24]. As a result, the CuO_x/CeO₂-NS(I) catalyst with exposed {111} and {100} facets possess the fewest oxygen vacancies, while the CuO_x/CeO₂-NW(I) with exposed {110} plane exhibits the most oxygen vacancies.

3.3. Chemical state, local coordination environment and redox behavior of CuO_x/CeO₂

To illustrate the surface composition and chemical state of copper species, surface sensitive XPS was conducted on the CuO_x/CeO₂(I) catalysts. The molar ratios of Cu to Ce on the surface for CuO_x/CeO₂-NR(I), CuO_x/CeO₂-NW(I), and CuO_x/CeO₂-NS(I) catalysts are 0.23, 0.30, and 0.19 (Table 1), respectively. Therein, the lower Cu/Ce molar ratio in the CuO_x/CeO₂-NS(I) is attributed to the highly dispersed CuO_x species in strong interaction with CeO₂ existed as the Cu-[O_x]-Ce.

Cu 2p XPS spectra (Fig. 4a) consist of two groups of peaks, including Cu 2p_{3/2} and Cu 2p_{1/2}. The characteristic peaks in a range of 932.8–933.5 eV are related to Cu⁰ or Cu⁺ species, and the peaks at 933.8 eV, accompanied with an intense shake-up satellite peak, are identified as Cu²⁺ species [25,26]. Satellite shake-up peaks existed in all samples indicates that the reduced copper species and Cu²⁺ coexist on the surface of as-synthesized CuO_x/CeO₂(I) catalysts. In more detail, the

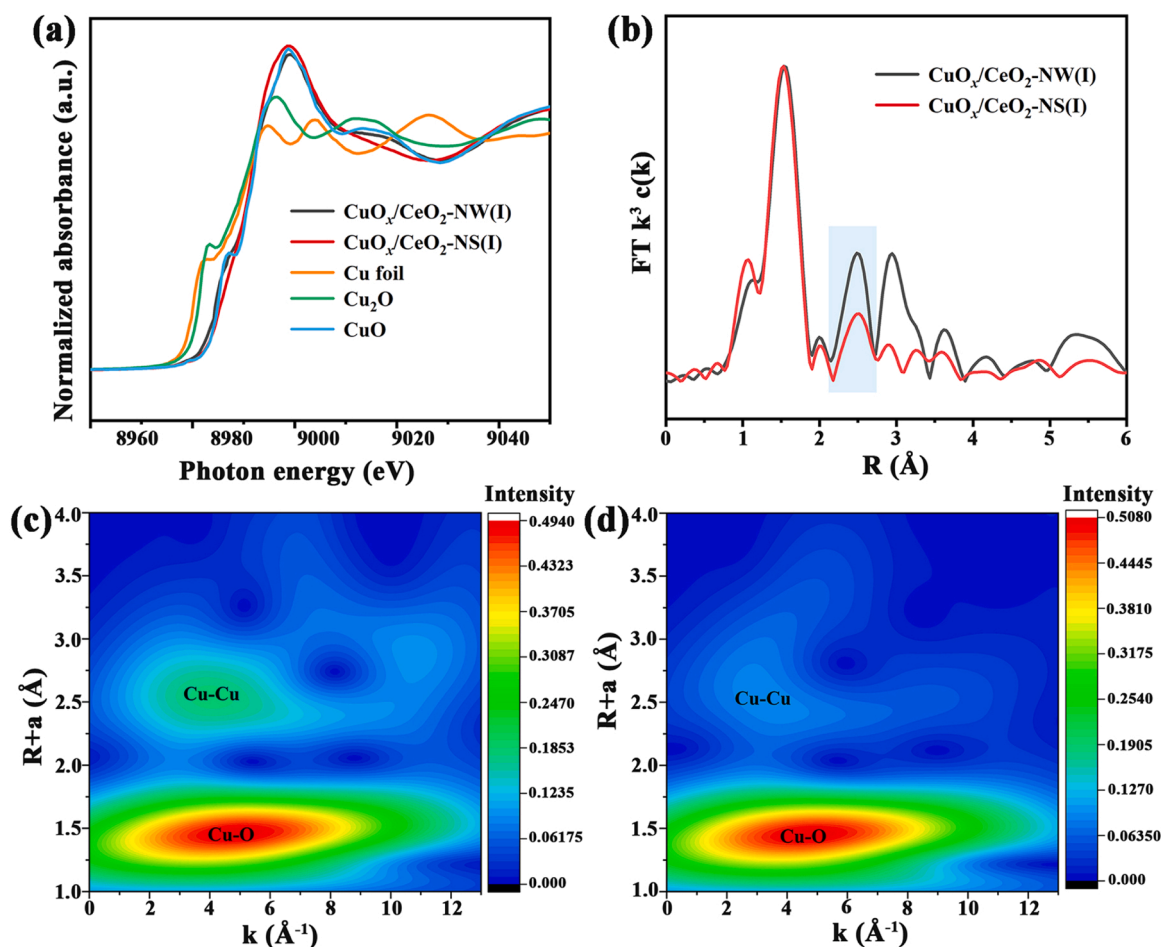


Fig. 5. Local Structure of the $\text{CuO}_x/\text{CeO}_2(\text{I})$ catalysts: (a) XANES spectra with Cu foil, Cu_2O and CuO as references; (b) EXAFS spectra at the R space of the given samples; the wavelet transformed XAS signals of (c) $\text{CuO}_x/\text{CeO}_2\text{-NW}(\text{I})$ and (d) $\text{CuO}_x/\text{CeO}_2\text{-NS}(\text{I})$.

degree of reduction of copper species was estimated by the ratio of the satellite peak intensity to the main peak intensity ($I_{\text{sat}}/I_{\text{mp}}$) [26,27]. In the case of $\text{CuO}_x/\text{CeO}_2\text{-NS}(\text{I})$, the $I_{\text{sat}}/I_{\text{mp}}$ value (Table 1) is the lowest relative to the pristine CuO and counterparts [27]. With the assistance of Cu Auger peak (Cu LMM) (Fig. S6), the reduced copper species are identified as Cu^+ . The relative population of Cu^+ species was estimated using the equation of $\text{Cu}^+ \% = [(A-(A1/B)B)/(A+B)] \times 100$ based on the literature reports [16,28]. Wherein, A is the area of the main Cu $2p_{3/2}$ peak (Fig. 4a), B is the area of the shake-up peak, and $(A1/B)$ is the ratio of the main peak/shake-up peak areas for a 100% pure Cu^{2+} sample (CuO). As shown in Table 1 and Fig. 4c, the proportion of surface Cu^+ follows the order of $\text{CuO}_x/\text{CeO}_2\text{-NS}(\text{I}) > \text{CuO}_x/\text{CeO}_2\text{-NR}(\text{I}) > \text{CuO}_x/\text{CeO}_2\text{-W}(\text{I})$, which is in good agreement with the previously discussed DFT calculations.

Fig. 4b displays Ce 3d XPS spectra of the $\text{CuO}_x/\text{CeO}_2(\text{I})$ catalysts, which were deconvoluted into five pairs of peaks. Wherein, three pairs of peaks centered at 882.5 and 900.8 eV, 888.2 and 907.4 eV as well as 897.9 and 916.4 eV are assigned to Ce $3d^{9/4} f^2 O 2p^4$ (v, u), Ce $3d^{9/4} f^1 O 2p^5$ (v', u') and Ce $3d^{9/4} f^0 O 2p^6$ (v'', u'') of Ce^{4+} , respectively [29,30]. The other two pairs of peaks at 885.0 and 903.1 eV as well as 880.8 and 890.6 eV, labeled as α , α' and β , β' , are related to Ce $3d_{5/2}$ and $3d_{3/2}$ of Ce^{3+} with Ce $3d^{9/4} f^1 O 2p^6$ and Ce $3d^{9/4} f^2 O 2p^5$ final states [30,31]. Based on the fitting results of XPS, the proportion of Ce^{3+} species associated with oxygen vacancies on the $\text{CuO}_x/\text{CeO}_2\text{-NW}(\text{I})$ is slightly higher than those on the other two samples (Table 1 and Fig. 4d), in accordance with the Raman results. As reported [10,32], the dopant of Cu or Cu ions in the CeO_2 lattice could result in the generation of charge-compensation oxygen vacancies. On the other hand, the Ce^{3+}

sites facilitate the exchange between surface oxygen species and gaseous oxygen, forming oxygen vacancies on the catalyst surface. The generation of oxygen vacancies results in charge imbalance, further induces the reduction of Ce^{4+} [9]. To explore whether Cu or Cu ions are incorporated into the lattice of CeO_2 , Rietveld refinement of XRD patterns was implemented. As shown in Fig. S7, there is no visible change in cell parameters of CeO_2 . Therefore, the formation of oxygen vacancies may be related to the presence of Ce^{3+} on the surface.

In view of the greatest differences in structure between $\text{CuO}_x/\text{CeO}_2\text{-NW}$ and $\text{CuO}_x/\text{CeO}_2\text{-NS}$, these two samples were selected for synchrotron radiation-based X-ray absorption fine structure (XAFS) experiments to illustrate the effect of the crystal plane on the local structure and the oxidation states of Cu species. Fig. 5a exhibits Cu K-edge X-ray absorption near-edge structure (XANES) spectra of the $\text{CuO}_x/\text{CeO}_2\text{-NW}(\text{I})$ and $\text{CuO}_x/\text{CeO}_2\text{-NS}(\text{I})$ catalysts, together with the references of Cu foil, Cu_2O , and CuO. More specifically, the white-line peak at 8997 eV, the shoulder peak at 8985 eV, and the pre-edge absorption at 8977 eV are all identified as the characteristics of Cu^{2+} , originating from the $1s \rightarrow 4p$ transition (continuum), $1s \rightarrow 4p_z$ transition (shakedown) and the $1s \rightarrow 3d$ transition, respectively [33]. As observed in Fig. 5a, the scattering oscillation of $\text{CuO}_x/\text{CeO}_2\text{-NW}(\text{I})$ and $\text{CuO}_x/\text{CeO}_2\text{-NS}(\text{I})$ at Cu k-edge is analogous to that of the CuO reference, signifying that copper species in these two catalysts is mainly present in the form of divalent copper. As depicted in the Fourier transform (FT) of the EXAFS (Fig. 5b), the dominant peak around 1.5 Å is ascribed to the first coordination shell of Cu-O, while another major peak at about 2.5 Å is attributed to the first Cu-Cu shell in the CuO [34]. In contrast, a significant difference is witnessed for the Cu-Cu coordination in the cases of the aforementioned

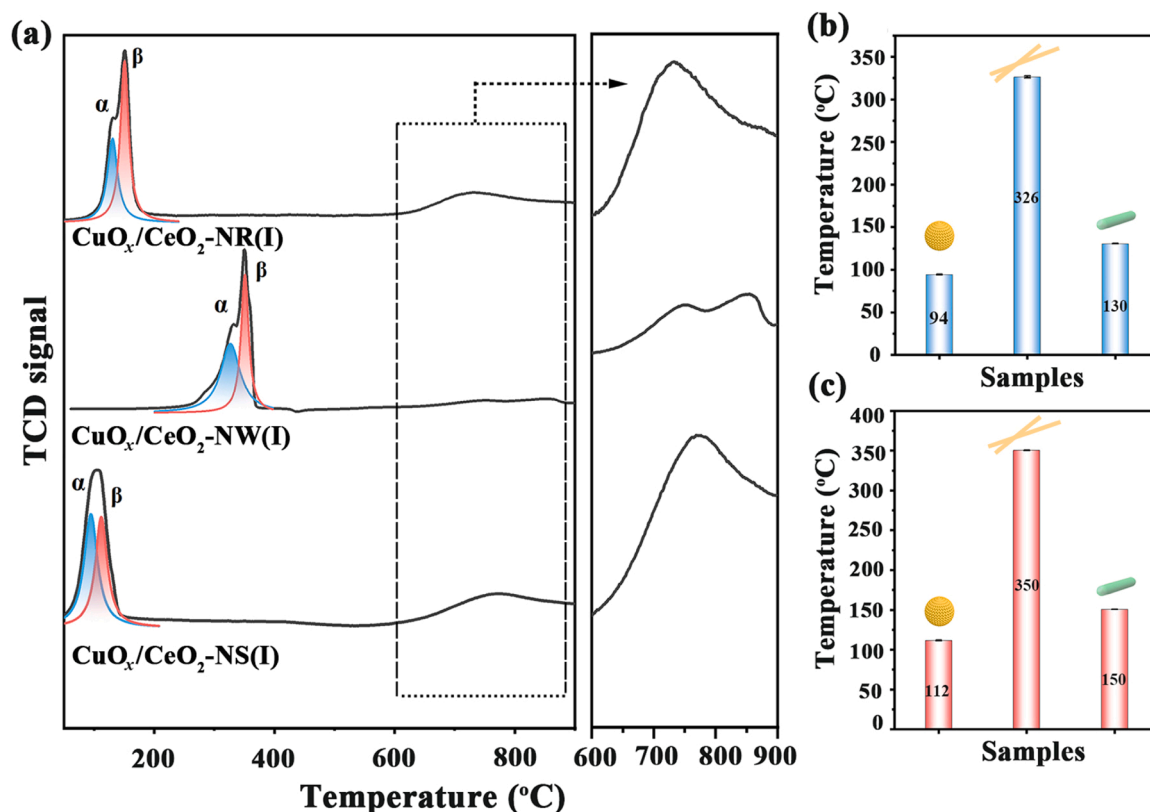


Fig. 6. Reduction behavior of the CuO_x/CeO₂(I) catalysts: (a) H₂-TPR profiles; Reduction temperatures of the peaks α (b) and peaks β (c).

two samples. In detail, the coordination number and the disorder factor (σ^2) of the Cu-Cu shell at ~ 2.50 Å obviously decrease in the CuO_x/CeO₂-NS(I) relative to that of the CuO_x/CeO₂-NW(I) (Fig. S8 and Table S2), validating the presence of more highly dispersed copper species in this catalyst [35,36]. The contour plots of wavelet transforms (WT)-EXAFS (Fig. 5c, d) provide clear visualizations of discrepancies in Cu-Cu coordination environment between the CuO_x/CeO₂-NW(I) and CuO_x/CeO₂-NS(I) catalysts.

H₂-TPR tests were carried out to estimate the dispersion of CuO_x species and the extent of overall catalyst reduction during the reduction process. As presented in Fig. 6a, the two-step reduction peaks are observed over all CuO_x/CeO₂(I) samples below 400 °C. Based on the reduction behavior and structural characteristics of the CuO_x/CeO₂(I), the first reduction peaks labelled as α are the most easily reduced CuO_x species, which are highly dispersed on the CeO₂ surface and have a strong interaction with supports [37]. And the second reduction peaks (β) at relatively higher temperature are attributed to the reduction of isolated CuO_x clusters weakly interacting with the CeO₂ [38]. The reduction temperatures of α and β peaks for CuO_x/CeO₂-NS(I) and CuO_x/CeO₂-NR(I) catalysts are much lower than that for CuO_x/CeO₂-NW(I) (Fig. 6a-c), especially for the CuO_x/CeO₂-NS(I). This observation indicates that the nanosphere-like CeO₂ supports are favorable for the formation of highly dispersed CuO_x species and the extraction of surface lattice oxygen species, in accordance with the results of DFT, XRD and EXAFS analyses. In addition to the strong reduction peaks below 400 °C, the reduction peaks at high temperature (600–900 °C) correspond to the reduction of bulk ceria [39,40]. Comparatively, the reduction peaks of bulk ceria for CuO_x/CeO₂-NS(I) are stronger than that for CuO_x/CeO₂-NW(I), corroborating a strong interaction between CuO_x and CeO₂ species in the CuO_x/CeO₂-NS(I) catalyst, in favor of the reduction of bulk ceria. Strong interaction between CuO_x and CeO₂ in CuO_x/CeO₂-NS(I) sample has been also verified by the lower reduction temperature of CeO₂ when compared to that of CeO₂-NS support (Fig. S9).

3.4. Catalytic performance of CuO_x/CeO₂ catalysts

Using CO-PROX as a prototype catalytic reaction, how CeO₂ crystal facets shape catalytic performance of the CuO_x/CeO₂ catalysts was evaluated in H₂-rich stream. Fig. 7a represents CO conversion and CO₂ selectivity over the CuO_x/CeO₂(I) catalysts during CO-PROX. To clearly illustrate catalytic activity, the temperatures of 10% ($T_{10\%}$), 50% ($T_{50\%}$) and 100% ($T_{100\%}$) CO conversion and temperature window are shown in Fig. 7b-c and Table 1. Comparatively, the catalytic activity follows the order of CuO_x/CeO₂-NS(I) > CuO_x/CeO₂-NR(I) > CuO_x/CeO₂-W(I). As revealed by Fig. S10, the reaction rates determined for CuO_x/CeO₂-NS(I) catalyst are $1.55 \times 10^{-3} \text{ mol}\cdot\text{s}^{-1}\cdot\text{m}^{-2}$ at 55 °C, $9.01 \times 10^{-3} \text{ mol}\cdot\text{s}^{-1}\cdot\text{m}^{-2}$ at 75 °C, respectively, which is all apparently higher than those for CuO_x/CeO₂-NW(I) ($2.05 \times 10^{-4} \text{ mol}\cdot\text{s}^{-1}\cdot\text{m}^{-2}$ at 55 °C and $2.51 \times 10^{-4} \text{ mol}\cdot\text{s}^{-1}\cdot\text{m}^{-2}$ at 75 °C). Meanwhile, the CuO_x/CeO₂-NS(I) catalyst processes wider temperature window for CO complete conversion than the traditional copper-cerium based catalysts reported in literature (Fig. 7c). These results are attributed the fact that the CeO₂-NS support with exposed {111} and {100} planes is favorable for anchoring the CuO_x active species on the surface, due to the strong adsorption energies for Cu₂O and CuO, resulting in the formation of highly dispersed CuO_x species, as evidenced from detailed XRD analysis, EXAFS fitting and DFT simulations. Highly dispersed CuO_x, especially Cu⁺, exposes more active sites to promote the surface reaction for CO oxidation. This is supported by a linear relationship between Cu⁺ content and the reaction rate (r) over the CuO_x/CeO₂(I) catalysts (Fig. S11). Intriguingly, the negative adsorption energies of Cu₂O and CuO on CeO₂ {100} and {111} facets also favor the interaction of the two components, improving the reduction of CuO_x and CeO₂. That is, the CuO_x-CeO₂ interfaces can efficiently boost catalytic performance at low temperatures. Note that the color of CuO_x/CeO₂-NS(I) sample changes after CO-PROX reaction (Fig. S12), which is related to the reduction of CuO_x during catalysis. Interestingly, after the used catalyst undergoes re-oxidation at 500 °C in air, it returns to its former color, indicating its

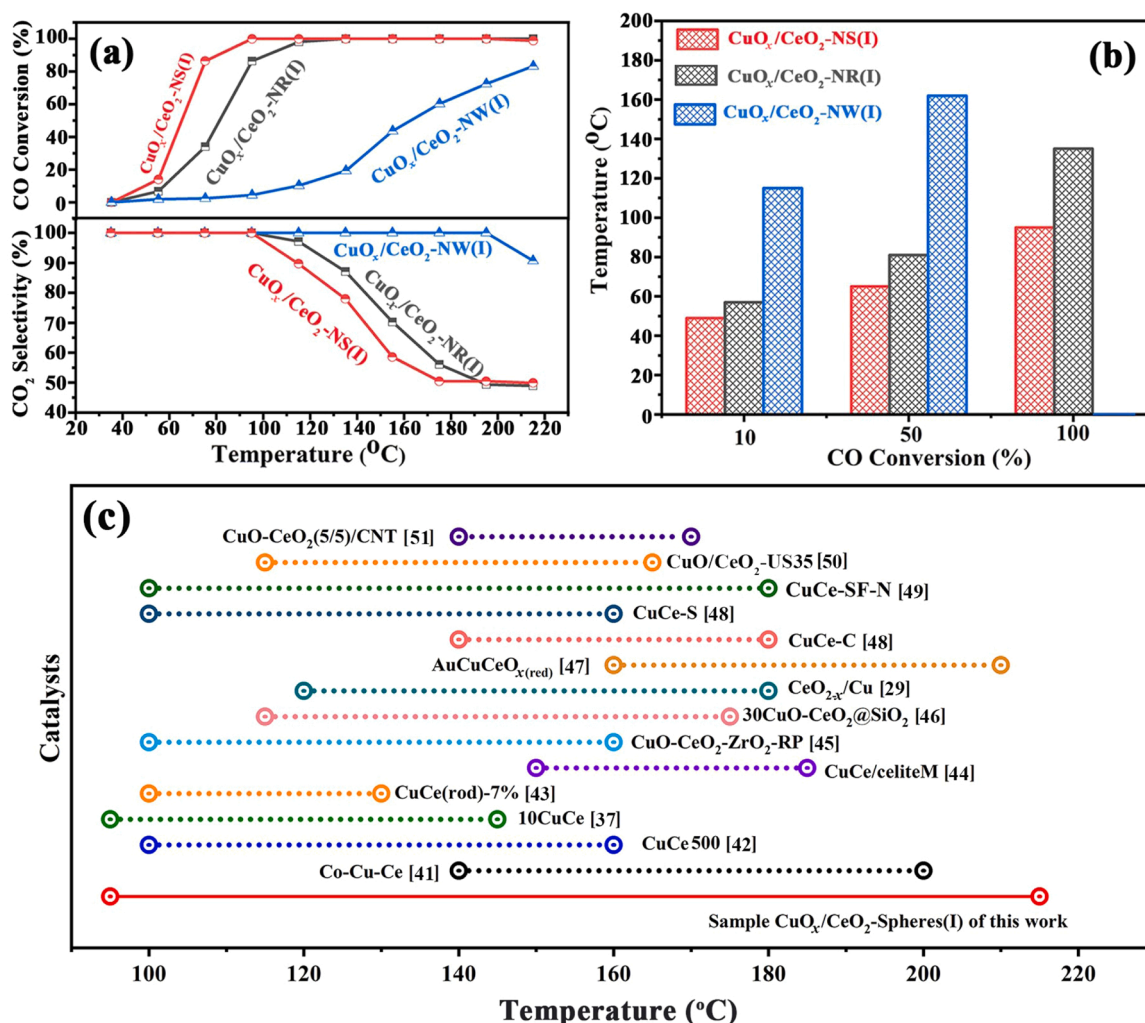


Fig. 7. Catalytic performance of the CO-PROX reaction over the CuO_x/CeO₂(I) catalysts: (a) CO conversion and CO₂ selectivity; (b) histogram of 10%, 50%, and 100% CO conversion versus reaction temperature; (c) comparison of the temperature window in this work and CuO_x-CeO₂ based catalysts reported in literatures [29, 37,41–51].

good reversibility. Additionally, as revealed by Fig. S13 and Fig. S14, the structure and morphology of CuO_x/CeO₂-NS(I) catalyst does not change significantly after the reaction, although its color changes, as confirmed above, which is associated with the reduction of copper oxides. Furthermore, the stability and reusability of CuO_x/CeO₂-NS(I) catalyst were evaluated. As presented in Fig. S15 and Fig. S16, the CuO_x/CeO₂-NS(I) possesses good reaction stability and reusability in the CO-PROX reaction.

3.5. Surface-dispersed active ingredient and structural evolution

To gain molecular-scale insights into the active sites and elucidate the detailed structure-activity relationship at CuO_x/CeO₂ interfaces, the active surface species and structural evolution were *in situ* studied under CO-PROX reaction condition. As shown in Fig. 8, DRIFTS spectra are divided into two characteristic regions, namely, the spectral zones in the range of 2400–2000 cm⁻¹ are assigned to the vibrational bands of CO₂ (g) and Cu^{II}-CO species, and the spectral zones from 1800 to 1200 cm⁻¹ are involved in the reaction intermediates such as carbonate, carboxyl or formate species [52]. For all CuO_x/CeO₂(I) catalysts, the strong vibrational features arising from Cu⁺-CO at 2140–2100 cm⁻¹ and the weak bands associated with Cu²⁺-CO at 2200–2140 cm⁻¹ are observed, signifying that surface-enriched Cu⁺ is the main active center for CO adsorption [53,54]. Of note, the intensity of Cu⁺-CO species increases as

the reaction temperature increases and reaches the maximum at about 110 °C. Further increasing the reaction temperature, the intensity of Cu⁺-CO band decreases, accompanied by the increase of CO₂ vibrational bands, which demonstrates the occurrence of redox reaction on the surface. Particularly, in the cases of CuO_x/CeO₂-NS(I) and CuO_x/CeO₂-NR(I), the Cu⁺-CO bands are located at 2100 cm⁻¹, while it appears at 2110 cm⁻¹ on the CuO_x/CeO₂-NW(I). It is proposed that the low-frequency Cu⁺-CO around 2100 cm⁻¹ corresponds to the smaller CuO_x with a strong interaction with CeO₂, and the high-frequency Cu⁺-CO vibration at 2110 cm⁻¹ is assigned to the larger CuO_x with a relatively weak interaction with CeO₂ [55,56]. The red shift of Cu⁺-CO stretching on the CuO_x/CeO₂-NS(I) and CuO_x/CeO₂-NR(I) signifies the presence of the smaller CuO_x on the catalyst surface and stronger synergistic interaction between two oxides relative to the CuO_x/CeO₂-NW(I), in agreement with the results of DFT, XRD, EXAFS and H₂-TPR.

In addition to the CO adsorption, the exposed crystal planes of CeO₂ supports also exert an influence on the reaction intermediates. As presented in Fig. 8, the peak at 1547 cm⁻¹ is carboxyl intermediate on the CuO_x/CeO₂-NS(I) catalyst [57,58], while the carbonates at 1348 cm⁻¹ and 1440 cm⁻¹ are main reaction intermediates for the CuO_x/CeO₂-NW(I) [59,60]. In the case of CuO_x/CeO₂-NR(I), the carboxyl and carbonates coexist on the surface. It is proposed that the deprotonation of the carboxyl intermediate generates CO₂ on the Pt/CeO₂ catalyst [61]. Besides, the presence of OH species assists the pathway of COOH on the

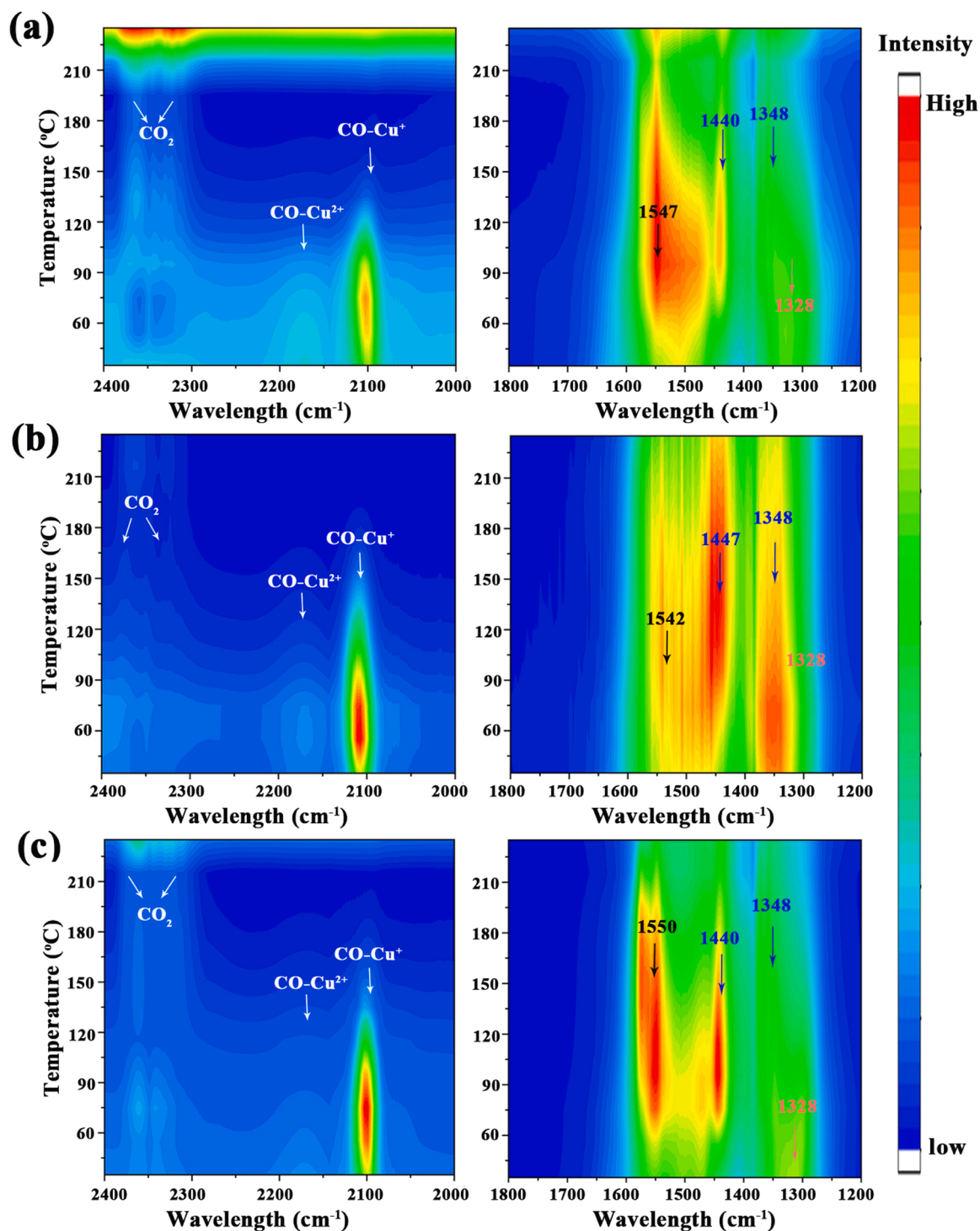


Fig. 8. *In situ* DRIFTS spectra over the catalysts under CO-PROX reaction condition (1% CO, 1% O₂, 50% H₂, He balance): (a) CuO_x/CeO₂-NS(I); (b) CuO_x/CeO₂-NW(I); (c) CuO_x/CeO₂-NR(I).

Pt/Al₂O₃ catalyst [62]. As shown in Fig. S17 and Table 1, the CuO_x/CeO₂-NS(I) possesses a higher concentration of hydroxyl relative to the counterparts. These phenomena can be explained that the CuO_x/CeO₂-NS(I) catalyst might follow the hydroxyl-assisted carboxyl pathway. Therefore, the carboxyl as an intermediate is easily decomposed at low temperature due to the presence of hydroxyl, whereas the carbonate accumulates on the surface, covering the active sites [63]. Based on the above analysis, it can be deduced that the CuO_x/CeO₂-NS(I) catalyst favors the CO adsorption and activation due to more exposed active sites and hydroxyl assistance during catalysis.

To investigate the structural evolution of samples during catalysis, *in situ* Raman spectroscopy was performed under CO-PROX reaction condition, which delivers direct evidence regarding the key intermediates and reaction pathways. Therein, The characteristic bands of fluorite-type CeO₂ phase at about 450 cm⁻¹ arise from the F_{2g} vibration mode of octahedral local symmetry, and the relatively weak bands at about 599 cm⁻¹ corresponding to defect-induced mode are observed in the CuO_x/CeO₂-NW(I) and CuO_x/CeO₂-NS(I) catalysts (Fig. 9a and b) at low temperature [21,22]. Red-shifting of the F_{2g} mode is attributed to the formation of oxygen vacancies and two-electron reduction [23]. As the

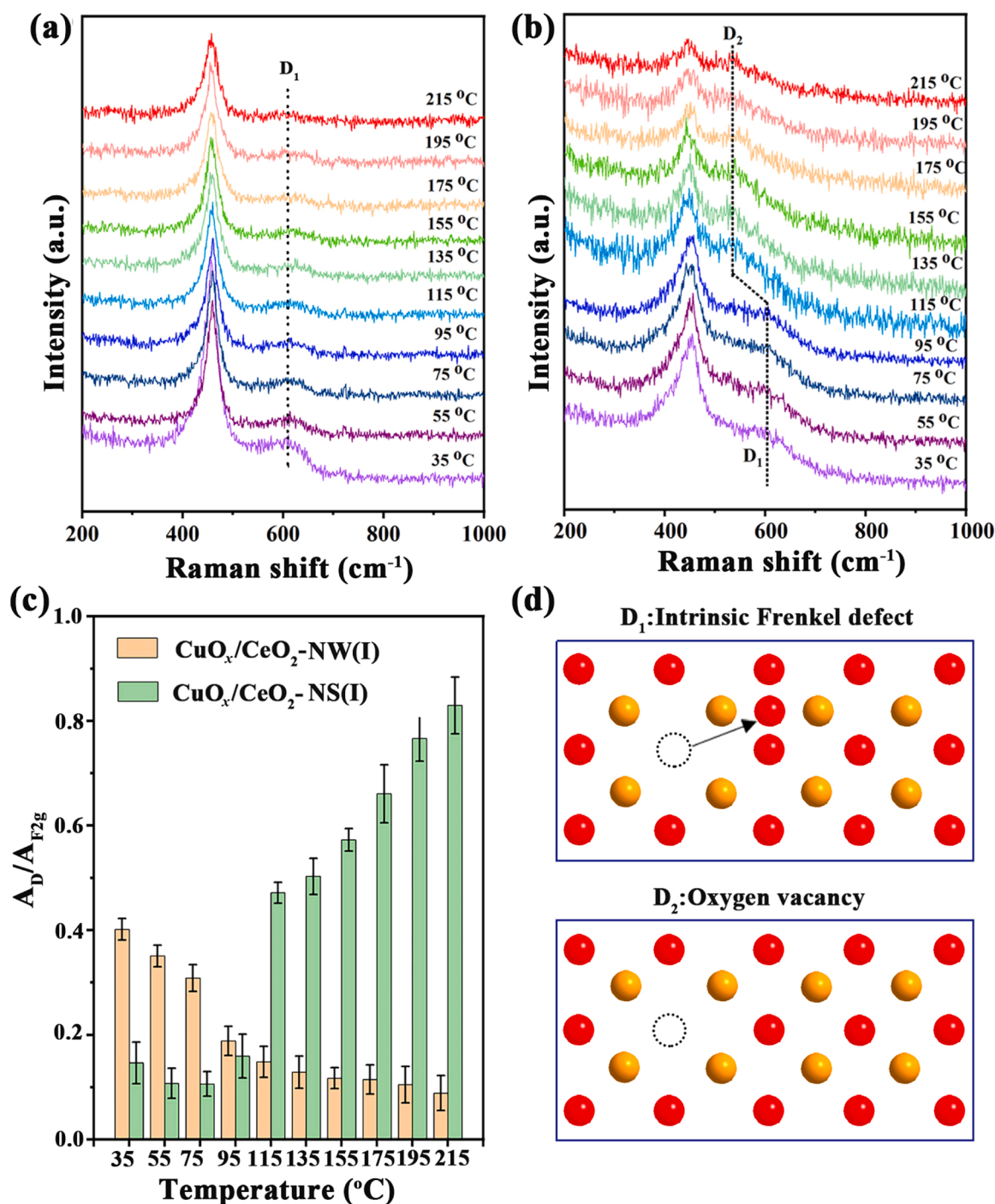


Fig. 9. *In situ* Raman spectra of (a) $\text{CuO}_x/\text{CeO}_2$ -NW(I) and (b) $\text{CuO}_x/\text{CeO}_2$ -NS(I) catalysts; (c) $A_{\text{D}}/A_{\text{F2g}}$ ratios at different temperatures; (d) the schematic structure of the defect sites (Ce: yellow ball; O: red ball).

temperature increases from 35° to 215°C, the intensity of $\text{F}_{2\text{g}}$ vibration gradually weakens on both catalysts, which is related to the disturbance of CeO_2 lattice during the heating process.

It is noteworthy that the $A_{\text{D}}/A_{\text{F2g}}$ ratio increases in the $\text{CuO}_x/\text{CeO}_2$ -NS(I), while this value decreases in the $\text{CuO}_x/\text{CeO}_2$ -NW(I) with the increase of temperature (Fig. 9c). It demonstrates that a large number of defects are generated on the $\text{CuO}_x/\text{CeO}_2$ -NS(I) surface originated from the reduction of surface ceria during the reaction, thus boosting O_2 activation at low temperature, in consistency with the results of CO-PROX activity. More importantly, the band at 599 cm^{-1} shifts to around 550 cm^{-1} on the $\text{CuO}_x/\text{CeO}_2$ -NS(I) at high temperature. Wherein, the D_1 peak at 599 cm^{-1} is linked to Frenkel-type defects

(Fig. 9d), in which a vacancy is generated by the displacement of an oxygen atom into an interstitial position [23,64]. The D_2 peak around 550 cm^{-1} is assigned to oxygen vacancy arising from the removal of an oxygen atom [65,66]. These results signify that oxygen on the $\text{CuO}_x/\text{CeO}_2$ -NS(I) surface is easily extracted and reacted with CO during catalysis, thus enhancing catalytic performance of the CO-PROX reaction.

3.6. Reaction mechanism of $\text{CuO}_x/\text{CeO}_2$ catalysts in CO-PROX

Taken together, Fig. 10 summarized the reaction mechanism of CO-PROX over the $\text{CuO}_x/\text{CeO}_2$ -NW(I) and $\text{CuO}_x/\text{CeO}_2$ -NS(I) catalysts. A

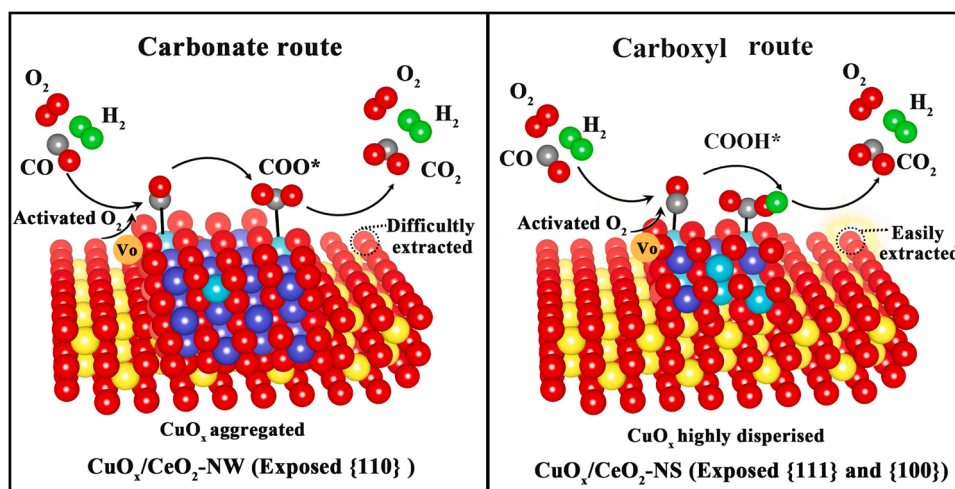


Fig. 10. Schematic diagram of the catalytic pathways over the $\text{CuO}_x/\text{CeO}_2$ with two morphologies under CO-PROX reaction (Ce: yellow ball; O: red ball; Cu^{2+} : blue ball; Cu^+ : cyan ball; oxygen vacancy: orange ball).

different mechanism can be linked to the $\text{CuO}_x\text{-CeO}_2$ interface. Computationally, theoretical simulations clearly reveal the intrinsic interaction between CuO_x and CeO_2 on the surface. Wherein, CeO_2 {100} and {111} planes are more favorable for stabilizing CuO_x species due to the strong adsorption energies, meanwhile, the E_{ads} values of Cu_2O on CeO_2 {100} and {111} surfaces are more negative relative to those of CuO , rendering the high dispersion of CuO_x and the presence of high proportion Cu^+ on the surface. Guided by the theoretical predication, we rationally designed the CeO_2 supports with the desired crystal planes. After impregnation of CuO_x active species, the structural features of the corresponding $\text{CuO}_x/\text{CeO}_2$ catalysts were systematically investigated by *ex situ* characterizations coupled with XAFS, *in situ* DRIFT and *in situ* Raman spectra.

Experimentally, HRTEM analyses demonstrate that the $\text{CeO}_2\text{-NW}$ exposed the {110} plane, the $\text{CeO}_2\text{-NR}$ exposed the {100} and {110} facets, while the $\text{CeO}_2\text{-NS}$ exposed the expected {100} and {111} planes. XRD, EDS, XPS, XAFS and TPR substantiates that the CuO_x species are highly dispersed on the $\text{CuO}_x/\text{CeO}_2\text{-NS(I)}$ surface. *In situ* DRIFTS together with *in situ* Raman spectra unravel that surface-enriched Cu^+ is the main active sites for CO adsorption. Meanwhile, the surface ceria is prone to reduce on the $\text{CuO}_x/\text{CeO}_2\text{-NS(I)}$ owing to synergistic interaction between CuO_x and CeO_2 species. A large number of defects are generated on the $\text{CuO}_x/\text{CeO}_2\text{-NS(I)}$ surface originated from the reduction of surface ceria during the reaction, thus boosting O_2 activation at low temperature. The coexistence of Frenkel-type defects and oxygen vacancies arising from the removal of oxygen atom signify that oxygen on the $\text{CuO}_x/\text{CeO}_2\text{-NS(I)}$ surface is easily extracted and reacted with CO during catalysis, enhancing catalytic performance of the CO-PROX reaction. That is, CeO_2 {111} surfaces are more favorable for stabilizing Cu_2O species, while CeO_2 {100} crystal planes are more conducive to the formation of oxygen vacancies [24]. They synergistically promote CO adsorption and oxygen species activation. It implicitly establishes an assumption that the exposure of specific facets can regulate the reactivity of supported CuO_x active species.

To further prove this hypothesis, we also tested the catalytic performance of three morphological $\text{CuO}_x/\text{CeO}_2$ catalysts synthesized by the hydrothermal method for contrast, which exhibits similarity toward activity of CO oxidation in comparison to those counterparts prepared by the aforementioned impregnation route (Fig. S18). Analogously, the supported CuO_x active species are highly distributed on the $\text{CuO}_x/\text{CeO}_2\text{-NR(H)}$ and $\text{CuO}_x/\text{CeO}_2\text{-NS(H)}$ catalysts, as evidenced by the XRD results (Fig. S19). As depicted in Fig. S20, S21 and Table S3, the morphologies and pore structure of CeO_2 supports are preserved after the hydrothermal process. More interestingly, three catalysts by the hydrothermal

method exhibit similar reduction behavior and surface reaction mechanism in contrast with the corresponding counterparts (Fig. S22 and S23). Facilitated by the similarity of crystal facets, these observations provide the reliable evidence that the dispersion of CuO_x is mainly related to the atomic arrangement of the CeO_2 supports.

On the basis of the coupled theoretical-experimental studies, the two reaction pathways for CO-PROX are proposed over the $\text{CuO}_x/\text{CeO}_2\text{-NW}$ (I) and $\text{CuO}_x/\text{CeO}_2\text{-NS(I)}$ catalysts (Fig. 10). In the case of nanowire-like catalyst, the formation of carbonate involves O_2 dissociation, CO activation and lattice oxygen extraction. Nevertheless, the generation of COOH^* intermediate is associated with CO activation, hydroxyl assistance and lattice oxygen extraction on the nanosphere sample. As aforementioned, oxygen in the CuO_x supported on the nanosphere-shaped CeO_2 surface is easily extracted and reacted with CO during catalysis. Finally, the COOH^* intermediates deprotonate to form CO_2 , and the adsorbed CO_2 desorbs from the Cu^+ sites to achieve the catalytic cycle.

4. Conclusions

In summary, the experiments, *in situ* characterization and first-principles calculations were integrated to elucidate the relationship of surface structure, reactant activation, catalytic performance and reaction mechanism of the $\text{CuO}_x/\text{CeO}_2$ catalysts for the CO-PROX reaction. DFT simulations indicates that CeO_2 {100} and {111} planes are more favorable for stabilizing Cu_2O species due to the strong adsorption energies, which have provided the first theoretical evidence for CuO_x adsorption and distribution on the different crystal facets of CeO_2 supports. XRD, $\text{H}_2\text{-TPR}$, XPS, XAFS and catalytic tests reveal that the optimal atomic arrangement appears on the nanosphere-shaped CeO_2 support with the exposed {111} and {100} facets with respect to its counterparts. More precisely, this optimal support configuration favors the formation of highly dispersed CuO_x and surface-enriched Cu^+ , which is highly active sites for CO-PROX reaction. As a consequence, these favorable features endow its superior catalytic performance. By combining *in situ* Raman and *in situ* DRIFTS spectra, it unravels the optimal support configuration facilitates lattice oxygen extraction, thus promoting the carboxyl pathway during the reaction. It is worth emphasizing that the insights into the influence of support configuration on active species dispersion and reactivity as well as the fundamental understanding of the synergetic effects give a clue on how to design an advanced heterogeneous catalyst.

CRediT authorship contribution statement

Junfang Ding: Conceptualization, Methodology, Formal analysis, Investigation, Data curation, Writing – original draft, Funding acquisition. **Changjin Xu:** Methodology, Formal analysis, Investigation, Writing – review & editing. **Guilan Fan:** Performing the theoretical calculations. **Tuya Naren:** Formal analysis, Investigation. **Yan Wang:** Validation, Formal analysis. **Yang Liu:** Validation, Formal analysis. **Xiaojun Gu:** Conceptualization, Formal analysis, Writing – review & editing, Funding acquisition. **Limin Wu:** Conceptualization, Formal analysis, Writing – review & editing. **Shanghong Zeng:** Conceptualization, Data curation, Formal analysis, Writing – review & editing, Funding acquisition, Resources, Supervision.

Declaration of Competing Interest

The authors declare that they have no known competing financial interests or personal relationships that could have appeared to influence the work reported in this paper.

Data Availability

No data was used for the research described in the article.

Acknowledgements

This work was financially supported by the National Natural Science Foundation of China (No. 21968020 and 22162019), the Natural Science Foundation of Inner Mongolia (2022MS02011, 2022QN02012, 2022QN02014), Science and Technology Projects of China Northern Rare Earth (BFXT-2022-D-0023) and the Science and Technology Projects of Inner Mongolia Autonomous Region (2021GG0195).

Appendix A. Supporting information

Supplementary data associated with this article can be found in the online version at doi:10.1016/j.apcatb.2023.122686.

References

- [1] Y. Li, W. Shen, Morphology-dependent nanocatalysts: rod-dhaped oxides, *Chem. Soc. Rev.* 43 (2014) 1543–1574.
- [2] Z. Li, S. Ji, Y. Liu, X. Cao, S. Tian, Y. Chen, Z. Niu, Y. Li, Well-defined materials for heterogeneous catalysis: from nanoparticles to isolated single-atom aites, *Chem. Rev.* 120 (2020) 623–682.
- [3] C. Xie, Z. Niu, D. Kim, M. Li, P. Yang, Surface and interface control in nanoparticle catalysis, *Chem. Rev.* 120 (2020) 1184–1249.
- [4] D. Wu, W. Baaziz, B. Gu, M. Marinova, W.Y. Hernández, W. Zhou, E.I. Vovk, O. Ersen, O.V. Safonova, A. Addad, N. Nuns, A.Y. Khodakov, V.V. Ordomsky, Surface molecular imprinting over supported metal catalysts for size-dependent selective hydrogenation reactions, *Nat. Catal.* 4 (2021) 595–606.
- [5] P. Ren, W. Tu, C. Wang, S. Cheng, W. Liu, Z. Zhang, Y. Tian, Y. Han, Mechanism and sites requirement for CO hydrogenation to CH₃OH over Cu/CeO₂ catalysts, *Appl. Catal. B Environ.* 305 (2022), 121016.
- [6] Y. Yan, R. Wong, Z. Ma, F. Donat, S. Xi, S. Saqline, Q. Fan, Y. Du, A. Borgna, Q. He, C.R. Müller, W. Chen, A.A. Lapkin, W. Liu, CO₂ hydrogenation to methanol on tungsten-doped Cu/CeO₂ catalysts, *Appl. Catal. B Environ.* 306 (2022), 121098.
- [7] X. Lai, Q. Xiao, C. Ma, W. Wang, C. Jia, Heterostructured ceria-titania-supported platinum catalysts for the water gas shift reaction, *ACS Appl. Mater. Interfaces* 14 (2022) 8575–8586.
- [8] Y. Xiao, H. Li, K. Xie, Activating lattice oxygen at the twisted surface in a mesoporous CeO₂ single crystal for efficient and durable catalytic CO oxidation, *Angew. Chem. Int. Ed.* 60 (2021) 5240–5244.
- [9] A. Davó-Quinónero, E. Bailón-García, S. López-Rodríguez, J. Juan-Juan, D. Lozano-Castelló, M. García-Melchor, F.C. Herrera, E. Pellegrin, C. Escudero, A. Bueno-López, Insights into the oxygen vacancy filling mechanism in CuO/CeO₂ catalysts: a key step toward high selectivity in preferential CO oxidation, *ACS Catal.* 10 (2020) 6532–6545.
- [10] B. Wang, H. Zhang, W. Xu, X. Li, W. Wang, L. Zhang, Y. Li, Z. Peng, F. Yang, Z. Liu, Nature of active sites on Cu-CeO₂ catalysts activated by high-temperature thermal aging, *ACS Catal.* 10 (2020) 12385–12392.
- [11] Z. Wu, H. Zhu, Z. Qin, H. Wang, J. Ding, L. Huang, J. Wang, CO preferential oxidation in H₂-rich stream over a CuO/CeO₂ catalyst with high H₂O and CO₂ tolerance, *Fuel* 104 (2013) 41–45.
- [12] Z. Liu, Q. Wang, J. Wu, H. Zhang, Y. Liu, T. Zhang, H. Tian, S. Zeng, Active sites and interfacial reducibility of Cu_xO/CeO₂ catalysts induced by reducing media and O₂/H₂ activation, *ACS Appl. Mater. Interfaces* 13 (2021) 35804–35817.
- [13] W. Wan, J. Geiger, N. Berdunov, M. Lopez Luna, S.W. Chee, N. Daelman, N. López, S. Shaikhutdinov, B. Roldan, Cuenya, Highly stable and reactive platinum single atoms on oxygen plasma-functionalized CeO₂ surfaces: nanostructuring and peroxo effects, *Angew. Chem. Int. Ed.* 61 (2022) e2021126.
- [14] D. Shen, Z. Li, J. Shan, G. Yu, X. Wang, Y. Zhang, C. Liu, S. Lyu, J. Li, L. Li, Synergistic Pt-CeO₂ interface boosting low temperature dry reforming of methane, *Appl. Catal. B Environ.* 318 (2022), 121809.
- [15] G. Vilé, S. Colussi, F. Krumeich, A. Trovarelli, J. Pérez-Ramírez, Opposite face sensitivity of CeO₂ in hydrogenation and oxidation catalysis, *Angew. Chem. Int. Ed.* 53 (2014) 12069–12072.
- [16] M. Lykaki, E. Pachatouridou, S.A.C. Carabineiro, E. Iliopoulou, C. Andriopoulou, N. Kallithrakas-Kontos, S. Boghosian, M. Konsolakis, Ceria nanoparticles shape effects on the structural defects and surface chemistry: implications in CO oxidation by Cu/CeO₂ catalysts, *Appl. Catal. B: Environ.* 230 (2018) 18–28.
- [17] M.J. Manto, P. Xie, C. Wang, Catalytic dephosphorylation using ceria nanocrystals, *ACS Catal.* 7 (2017) 1931–1938.
- [18] Y. Xie, J. Wu, G. Jing, H. Zhang, S. Zeng, X. Tian, X. Zou, J. Wen, H. Su, C. Zhong, P. Cui, Structural origin of high catalytic activity for preferential CO oxidation over CuO/CeO₂ nanocatalysts with different ashapes, *Appl. Catal. B Environ.* 239 (2018) 665–676.
- [19] X. Yang, Q. Li, E. Lu, Z. Wang, X. Gong, Z. Yu, Y. Guo, L. Wang, Y. Guo, W. Zhan, J. Zhang, S. Dai, Taming the stability of Pd active phases through a compartmentalizing strategy toward nanostructured catalyst supports, *Nat. Commun.* 10 (2019) 1611.
- [20] F. Hu, R. Ye, C. Jin, D. Liu, X. Chen, C. Li, K.H. Lim, G. Song, T. Wang, G. Feng, R. Zhang, S. Kawi, Ni nanoparticles enclosed in highly mesoporous nanofibers with oxygen vacancies for efficient CO₂ methanation, *Appl. Catal. B Environ.* 317 (2022), 121715.
- [21] Z. Zhang, Y. Wang, J. Lu, J. Zhang, M. Li, X. Liu, F. Wang, Pr-doped CeO₂ catalyst in the prins condensation-hydrolysis reaction: are all of the defect sites catalytically active? *ACS Catal.* 8 (2018) 2635–2644.
- [22] Z. Xiao, Y. Li, F. Hou, C. Wu, L. Pan, J. Zou, L. Wang, X. Zhang, G. Liu, G. Li, Engineering oxygen vacancies and nickel dispersion on CeO₂ by Pr doping for highly stable ethanol steam reforming, *Appl. Catal. B Environ.* 258 (2019), 117940.
- [23] S. Agarwal, X. Zhu, E.J.M. Hensen, B.L. Mojet, L. Lefferts, Surface-dependence of defect chemistry of nanostructured ceria, *J. Phys. Chem. C* 119 (2015) 12423–12433.
- [24] A. Trovarelli, J. Llorca, Ceria catalysts at nanoscale: how do crystal shapes shape catalysis? *ACS Catal.* 7 (2017) 4716–4735.
- [25] A. Davó-Quinónero, I. Such-Basáñez, J. Juan-Juan, D. Lozano-Castelló, P. Stelmachowski, G. Grzybek, A. Kotarba, A. Bueno-López, New insights into the role of active copper species in CuO/cryptomelane catalysts for the CO-PROX reaction, *Appl. Catal. B Environ.* 267 (2020), 118372.
- [26] J. Ding, L. Li, H. Li, S. Chen, S. Fang, T. Feng, G. Li, Optimum preferential oxidation performance of CeO₂-CuO_x-RGO composites through interfacial regulation, *ACS Appl. Mater. Interfaces* 10 (2018) 7935–7945.
- [27] J. Hou, J. Hu, L. Chang, J. Wang, Z. Zeng, D. Wu, X. Cui, W. Bao, J. Yao, Synergistic effects between highly dispersed CuO_x and the surface Cu-[O₂]-Ce structure on the catalysis of benzene combustion, *J. Catal.* 408 (2022) 9–23.
- [28] M. Biesinger, L. Lau, A. Gerson, R. Smart, Resolving surface chemical states in XPS analysis of first row transition metals, oxides and hydroxides: Sc, Ti, V, Cu and Zn, *Appl. Surf. Sci.* 257 (2010) 887–898.
- [29] S. Chen, L. Li, W. Hu, X. Huang, Q. Li, Y. Xu, Y. Zuo, G. Li, Anchoring high-concentration oxygen vacancies at interfaces of CeO₂/Cu toward enhanced activity for preferential CO oxidation, *ACS Appl. Mater. Interfaces* 7 (2015) 22999–23007.
- [30] F. Zhang, P. Wang, J. Koberstein, S. Khalid, S.W. Chan, Cerium oxidation state in ceria nanoparticles studied with X-ray photoelectron spectroscopy and absorption near edge spectroscopy, *Surf. Sci.* 563 (2004) 74–82.
- [31] J.P. Holgado, G. Munuera, J.P. Espinós, A.R. González-Elipe, XPS study of oxidation processes of CeO_x defective layers, *Appl. Surf. Sci.* 158 (2000) 164–171.
- [32] X. Zhang, P. Tian, W. Tu, Z. Zhang, J. Xu, Y. Han, Tuning the dynamic interfacial structure of copper-ceria catalysts by indium oxide during CO oxidation, *ACS Catal.* 8 (2018) 5261–5275.
- [33] S. Zhang, H. Li, P. Liu, L. Ma, L. Li, W. Zhang, F. Meng, L. Li, Z. Yang, T. Wu, F. Huo, J. Lu, Directed self-assembly of MOF-derived nanoparticles toward hierarchical structures for enhanced catalytic activity in CO oxidation, *Adv. Energy Mater.* 9 (2019) 1–7.
- [34] C. Pan, C. Wang, X. Zhao, P. Xu, F. Mao, J. Yang, Y. Zhu, R. Yu, S. Xiao, Y. Fang, H. Deng, Z. Luo, J. Wu, J. Li, S. Liu, S. Xiao, L. Zhang, Y. Guo, Neighboring Sp-hybridized carbon participated molecular oxygen activation on the interface of sub-nanocluster CuO/graphdiyne, *J. Am. Chem. Soc.* 144 (2022) 4942–4951.
- [35] F. Han, M. Yuan, S. Mine, H. Sun, H. Chen, T. Toyao, M. Matsuoka, K. Zhu, J. Zhang, W. Wang, T. Xue, Formation of highly active superoxide sites on CuO nanoclusters encapsulated in SAPO-34 for catalytic selective ammonia oxidation, *ACS Catal.* 9 (2019) 10398–10408.
- [36] A. Tschöpe, J. Markmann, P. Zimmer, R. Birringer, A.V. Chadwick, N₂O temperature-programmed oxidation and EXAFS studies on the dispersion of copper in ceria-supported nanocatalysts, *Chem. Mater.* 17 (2005) 3935–3943.
- [37] Z. Qiu, X. Guo, J. Mao, R. Zhou, Elucidating the structure, redox properties and active entities of high-temperature thermally aged CuO_x-CeO₂ catalysts for CO-PROX, *Phys. Chem. Chem. Phys.* 23 (2021) 15582–15590.

- [38] J. Yu, Q. Guo, X. Xiao, H. Mao, D. Mao, J. Yu, High-heat treatment enhanced catalytic activity of CuO/CeO₂ catalysts with low CuO content for CO oxidation, *Catal. Sci. Technol.* 10 (2020) 5256–5266.
- [39] Y. Gao, Z. Zhang, Z. Li, W. Huang, Understanding morphology-dependent CuO_x-CeO₂ interactions from the very beginning, *Chin. J. Catal.* 41 (2020) 1006–1016.
- [40] O.H. Laguna, W.Y. Hernández, G. Arzamendi, L.M. Gandía, M.A. Centeno, J. A. Odriozola, Gold supported on CuO_x/CeO₂ catalyst for the purification of hydrogen by the CO preferential oxidation reaction (PROX), *Fuel* 118 (2014) 176–185.
- [41] J.L. Ayastuy, E. Fernández-Puertas, M.P. González-Marcos, M.A. Gutiérrez-Ortiz, Transition metal promoters in CuO/CeO₂ catalysts for CO removal from hydrogen streams, *Int. J. Hydrog. Energy* 37 (2012) 7385–7397.
- [42] C. Wang, Q. Cheng, X. Wang, K. Ma, X. Bai, S. Tan, Y. Tian, T. Ding, L. Zheng, J. Zhang, X. Li, Enhanced catalytic performance for CO preferential oxidation over CuO catalysts supported on highly defective CeO₂ nanocrystals, *Appl. Surf. Sci.* 422 (2017) 932–943.
- [43] X. Guo, Z. Qiu, J. Mao, R. Zhou, Shape-controlled Cu₃Ce_{1-x}O₂ nanorods catalyst and the active components functioned in selective oxidation of CO in hydrogen-rich stream, *J. Power Sources* 451 (2020), 227757.
- [44] I.S. Tiscornia, A.M. Lacoste, L.E. Gómez, A.V. Boix, CuO-CeO₂/SiO₂ coating on ceramic monolith: effect of the nature of the catalyst support on CO preferential oxidation in a H₂-rich stream, *Int. J. Hydrog. Energy* 45 (2020) 6636–6650.
- [45] L. Shi, G. Zhang, Improved low-temperature activity of CuO-CeO₂-ZrO₂ catalysts for preferential oxidation of CO in H₂-rich streams, *Catal. Lett.* 146 (2016) 1449–1456.
- [46] H. Zhang, X. Zhao, S. Wang, S. Zeng, H. Su, Change of Cu⁺ species and synergistic effect of copper and cerium during reduction-oxidation treatment for preferential CO oxidation, *Appl. Surf. Sci.* 441 (2018) 754–763.
- [47] J. Papavasiliou, Interaction of atomically dispersed gold with hydrothermally prepared copper-cerium oxide for preferential CO oxidation reaction, *Catal. Today* 357 (2020) 684–693.
- [48] Q. Zou, Y. Zhao, X. Jin, J. Fang, D. Li, K. Li, J. Lu, Y. Luo, Ceria-nano supported copper oxide catalysts for CO preferential oxidation: importance of oxygen species and metal-support interaction, *Appl. Surf. Sci.* 494 (2019) 1166–1176.
- [49] J. Wang, H. Pu, G. Wan, K. Chen, J. Lu, Y. Lei, L. Zhong, S. He, C. Han, Y. Luo, Promoted the reduction of Cu²⁺ to enhance CuO-CeO₂ catalysts for CO preferential oxidation in H₂-rich streams: effects of preparation methods and copper precursors, *Int. J. Hydrog. Energy* 42 (2017) 21955–21968.
- [50] Y. Xia, J. Lao, J. Ye, D. Cheng, F. Chen, X. Zhan, Role of two-electron defects on the CeO₂ surface in CO preferential oxidation over CuO/CeO₂ catalysts, *ACS Sustain. Chem. Eng.* 7 (2019) 18421–18433.
- [51] Y. Gao, K. Xie, W. Wang, S. Mi, N. Liu, G. Pan, W. Huang, Structural features and catalytic performance in CO preferential oxidation of CuO-CeO₂ supported on multi-walled carbon nanotubes, *Catal. Sci. Technol.* 5 (2015) 1568–1579.
- [52] C. Ma, C. Yang, B. Wang, C. Chen, F. Wang, X. Yao, M. Song, Effects of H₂O on HCHO and CO oxidation at room-temperature catalyzed by MCo₂O₄ (M=Mn, Ce and Cu) materials, *Appl. Catal. B Environ.* 254 (2019) 76–85.
- [53] M. Monte, D. Gamarra, A. López Cámara, S. Rasmussen, N. Gyorffy, Z. Schay, A. Martínez-Arias, J. Conesa, Preferential oxidation of CO in excess H₂ over CuO/CeO₂ catalysts: performance as a function of the copper coverage and exposed face present in the CeO₂ support, *Catal. Today* 229 (2014) 104–113.
- [54] R. Kydd, D. Ferri, P. Hug, J. Scott, W. Teoh, R. Amal, Temperature-induced evolution of reaction sites and mechanisms during preferential oxidation of CO, *J. Catal.* 277 (2011) 64–71.
- [55] X. Guo, R. Zhou, A new insight into the morphology effect of ceria on CuO/CeO₂ catalysts for CO selective oxidation in hydrogen-rich gas, *Catal. Sci. Technol.* 6 (2016) 3862–3871.
- [56] D. Gamarra, C. Belver, M. Fernández-García, A. Martínez-Arias, Selective CO oxidation in excess H₂ over copper-ceria catalysts: identification of active entities/species, *J. Am. Chem. Soc.* 129 (2007) 12064–12065.
- [57] S. Kattel, B. Yan, Y. Yang, J. Chen, P. Liu, Optimizing binding energies of key intermediates for CO₂ hydrogenation to methanol over oxide-supported copper, *J. Am. Chem. Soc.* 138 (2016) 12440–12450.
- [58] K. Bando, K. Sayama, H. Kusama, K. Okabe, H. Arakawa, In-situ FT-IR study on CO₂ hydrogenation over Cu catalysts supported on SiO₂, Al₂O₃, and TiO₂, *Appl. Catal. A Gen.* 165 (1997) 391–409.
- [59] D. Gamarra, G. Munuera, A.B. Hungri, M. Ferna, A. Marti, Structure-activity relationship in nanostructured copper-ceria-based preferential CO oxidation catalysts, *J. Phys. Chem. C* 111 (2007) 11026–11038.
- [60] H. Li, L. Li, S. Fang, J. Wang, S. Chen, X. Huang, Z. Leng, G. Li, Surface hydroxylation induced by alkaline-earth metal doping in NiO nanocrystals and its application in achieving a wide temperature operation window for preferential CO oxidation, *Environ. Sci. Nano* 5 (2018) 2368–2381.
- [61] L. Nie, D. Mei, H. Xiong, B. Peng, Z. Ren, X. Hernandez, A. DeLaRiva, M. Wang, M. Engelhard, L. Kovarik, A. Datye, Y. Wang, Activation of surface lattice oxygen in single-atom Pt/CeO₂ for low-temperature CO oxidation, *Science* 358 (2017) 1419–1423.
- [62] Y. Chen, Y. Feng, L. Li, J. Liu, X. Pan, W. Liu, F. Wei, Y. Cui, B. Qiao, X. Sun, X. Li, J. Lin, S. Lin, X. Wang, T. Zhang, Identification of active sites on high-performance Pt/Al₂O₃ catalyst for cryogenic CO oxidation, *ACS Catal.* 10 (2020) 8815–8824.
- [63] A. Davó-Quinonero, M. Navlani-García, D. Lozano-Castelló, A. Bueno-López, J. Anderson, Role of hydroxyl groups in the preferential oxidation of CO over copper oxide-cerium oxide catalysts, *ACS Catal.* 6 (2016) 1723–1731.
- [64] S. Agarwal, X. Zhu, E. Hensen, L. Lefferts, B. Mojet, Defect chemistry of ceria nanorods, *J. Phys. Chem. C* 118 (2014) 4131–4142.
- [65] A. Filtschew, K. Hofmann, C. Hess, Ceria and its defect structure: new insights from a combined spectroscopic approach, *J. Phys. Chem. C* 120 (2016) 6694–6703.
- [66] E. Sartoretti, C. Novara, M. Fontana, F. Giorgis, M. Piumetti, S. Bensaid, N. Russo, D. Fino, New insights on the defect sites evolution during CO oxidation over doped ceria nanocatalysts probed by in situ Raman spectroscopy, *Appl. Catal. A Gen.* 596 (2020), 117517.